ISSN 1029-9599, Physical Mesomechanics, 2022, Vol. 25, No. 5, pp. 385–392. © Pleiades Publishing, Ltd., 2022.
Russian Text © The Author(s), 2022, published in Fizicheskaya Mezomekhanika, 2022, Vol. 25, No. 3, pp. 5–14.

Strain Rate and Temperature Effects on Hydrogen Embrittlement of Stable and Metastable High-Entropy Alloys

M. Koyama[1,2]*, K. Ichii[3], and K. Tsuzaki[1,2,3,4]

[1] *Institute for Materials Research, Tohoku University, Sendai, 980-8577 Japan*
[2] *Elements Strategy Initiative for Structural Materials, Kyoto University, Kyoto, 606-8501 Japan*
[3] *Faculty of Engineering, Kyushu University, Fukuoka, 819-0395 Japan*
[4] *Research Center for Structural Materials, National Institute for Materials Science, Tsukuba, 305-0047 Japan*
** e-mail: motomichi.koyama.c5@tohoku.ac.jp, koyama@imr.tohoku.ac.jp*

Received January 31, 2022; revised January 31, 2022; accepted March 31, 2022

Abstract—The strain rate and temperature effects on the hydrogen embrittlement behavior of Fe-20Mn-20Ni-20Cr-20Co and Fe-30Mn-10Cr-10Co (at %) high-entropy alloys were investigated. The Fe-20Mn-20Ni-20Cr-20Co high-entropy alloy exhibits a mechanically stable face-centered cubic (FCC) structure. The as-annealed microstructure of the Fe-30Mn-10Cr-10Co high-entropy alloy consists of a metastable FCC phase with a thermally induced hexagonal close-packed (HCP) martensite. After hydrogen precharging in a 100-MPa hydrogen gas atmosphere, tensile tests were carried out on the two high-entropy alloys. The hydrogen increased the yield strength of both alloys. With the increase in strain rate from 10^{-4} to 10^{-2} s^{-1}, the yield strength of the hydrogen-charged Fe-20Mn-20Ni-20Cr-20Co alloy markedly increased, which indicates activation of the strengthening mechanism related to the thermal activation of dislocation motion associated with hydrogen atoms. In contrast, the strain rate effect on the yield strength was insignificant in the Fe-30Mn-10Cr-10Co alloy, where the FCC–HCP martensitic transformation dominated the onset of plasticity. In terms of failure, the combined hydrogen effects that increased the flow stress and decreased the work-hardening rate in the late deformation stage accelerated the occurrence of specimen necking, particularly at a high strain rate, e.g. 10^{-2} s^{-1} at 20°C. In addition, the elongation of the hydrogen-charged Fe-20Mn-20Ni-20Cr-20Co and Fe-30Mn-10Cr-10Co alloys increased with the strain rate, which indicates that the hydrogen transport by dislocation motion in late deformation stages assisted both modes of cracking (along grain boundaries and HCP martensite plates) in high-entropy alloys, which resulted in hydrogen-induced intergranular fracture and quasi-cleavage fracture, particularly at relatively low strain rates. Importance of the hydrogen transport by dislocation motion for brittle fracture at 20°C was supported by the test results at –100°C: brittle fracture occurred at higher stress and larger strain as compared to the cases at 20°C for both alloys.

Keywords: hydrogen embrittlement, high-entropy alloy, strain rate, deformation temperature, fracture surface

DOI: 10.1134/S1029959922050010

1. INTRODUCTION

High-strength alloys with significant resistance to hydrogen have been explored to achieve light, safe, and long-lifetime infrastructures for hydrogen energy. However, the hydrogen embrittlement susceptibility increases with increasing strength level, which is a dilemma in this issue. In this context, face-centered cubic (FCC) alloys, such as austenitic steel and Ni alloys, are considered to be hydrogen-resistant materials. To obtain hydrogen-resistant FCC alloys, the deformation-induced martensitic transformation from FCC to body-centered cubic (BCC) structures must be suppressed [1]. However, mechanically stable FCC alloys generally exhibit low strength [2].

A pathway to increase the strength in mechanically stable FCC alloys is the high-entropy alloy (HEA) design strategy. The equiatomic composition of CoCr FeMnNi alloy exhibits a mechanically stable FCC structure, high toughness, and relatively high strength [3, 4]. In this study, stable FCC HEA is referred to as S-HEA. S-HEA exhibited a high resistance to hydrogen embrittlement [5–7]. However, hydrogen embrit-

tlement occurred when an S-HEA specimen was exposed to a 100-MPa hydrogen gas [8, 9]. Although hydrogen embrittlement can be suppressed by grain refinement [10] and removal of Mn [11, 12], the intrinsic cause of hydrogen embrittlement has not been clarified. Another pathway is the use of martensitic transformation from the FCC to hexagonal close-packed (HCP) structure for increasing the strength with a significant resistance to hydrogen embrittlement [13], because the HCP phase exhibits a low hydrogen diffusivity similar to that of the FCC phase [14]. As HEAs without Ni can exhibit the FCC → HCP martensitic transformation [15, 16], metastable HEA with the FCC → HCP transformation is another candidate for high-strength FCC-based alloys. In this study, metastable HEA is referred to as M-HEA. Hydrogen embrittlement of M-HEA hydrogen-charged with a 100-MPa hydrogen gas has been reported, although it occurred after a significant plastic deformation [9]. Therefore, to develop high-strength hydrogen-resistant FCC alloys, the factors affecting the embrittlement behavior must be elucidated through systematic experiments.

An important factor as a characteristic of the hydrogen embrittlement of HEAs is their strain-rate sensitivity. Similar to the hydrogen embrittlement behavior of other alloys, for both S-HEA and M-HEA, the elongation decreased with decreasing strain rate [17]. In addition, the work-hardening behavior seems to differ with the variation in strain rate. As the strain-rate sensitivity of HEAs has not been investigated in detail, the stress–strain response and fracture surfaces with different strain rates were thoroughly analyzed in this study, as the macroscopic and mesoscopic mechanical characterization. Furthermore, to deepen our understanding, the hydrogen embrittlement behavior at a low temperature of –100°C was investigated.

2. EXPERIMENTAL METHODS

The nominal chemical compositions of S-HEA and M-HEA used in this study were Fe-20Mn-20Ni-20Cr-20Co and Fe-30Mn-10Cr-10Co (at %). S-HEA was mechanically stable even after tensile fracture at ambient temperature and in cryogenic temperature [4]. M-HEA exhibits the transformation-induced plasticity effect originating from the martensitic transformation from the FCC to HCP structure [15, 16]. Ingots (50 kg) of the two alloys were prepared by vacuum induction melting and hot-rolled to a thickness of 52% at 1000°C followed by homogenization at 1200°C for 2 h in an Ar atmosphere and furnace cooling. The homogenized bars were further hot-rolled to obtain a thickness reduction to 33% (from 60 to 20 mm). The rolled bar was solution-treated at 800°C in an air atmosphere for 1 h, followed by water quenching. Tensile specimens with the 1 mm thickness were made by electric discharge machining. The gauge length and width of the specimens were 10 and 2 mm, respectively. To introduce hydrogen, the specimens were exposed to a 100-MPa hydrogen gas atmosphere at 270°C for 200 h. Tensile tests were carried out at ambient temperature (20°C) at the initial strain rates 10^{-4}, 10^{-3}, and 10^{-2} s^{-1}. Fracture surfaces were studied by scanning electron microscopy at the acceleration voltage 15 kV. The measured content of diffusion hydrogen in S-HEA and M-HEA was 113 and 178 ppm by mass, respectively [9].

3. RESULTS

3.1. Stable HEA

Figure 1 shows the nominal stress–strain curves of S-HEA without and with hydrogen charging. As reported previously, the yield strength increased by hydrogen charging owing to solution hardening and with the increase in strain rate. In addition, hydrogen decreased the work-hardening rate and elongation, irrespective of the strain rate. As shown in Fig. 1b, fracture of a hydrogen-charged specimen with the strain rate 10^{-2} s^{-1} occurred at the necking condition: $d\sigma/d\varepsilon = \sigma$, where σ and ε are the true stress and true strain, respectively.

Figure 2 shows fractographs of hydrogen-charged specimens obtained after the tensile tests (Fig. 1). The entire region of the fracture surfaces exhibited brittle features (Figs. 2a–2c). The major portion of the fracture surfaces showed features of intergranular fracture, irrespective of the strain rate; i.e. no significant changes appeared in the fractographic features when the strain rate was changed.

Figure 3 shows the deformation behavior when the deformation temperature changes from 20 to –100°C. A decrease in temperature decreases the stacking fault energy of the FCC structure, which promotes deformation twinning in FCC alloys, including S-HEA [18]. The promoted deformation twinning increases the work-hardening rate and the associated uniform elongation when hydrogen is not introduced. The deformation behavior at –100°C without hydrogen charging followed the conventional trend. Hydrogen charging decreased the elongation but increased the work-hardening rate at –100°C,

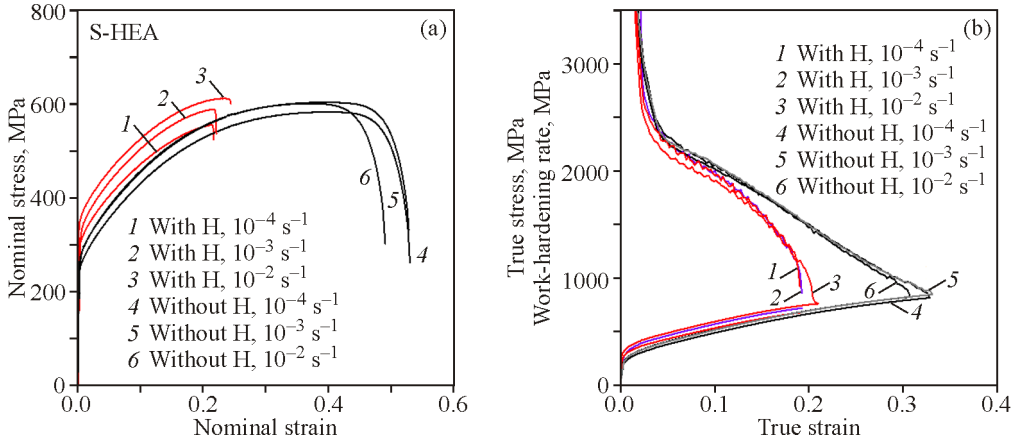

Fig. 1. Nominal stress–strain (a) and work-hardening rate curves at 20°C with (*1–3*) and without (*4–6*) hydrogen charging (H) in S-HEA (b). Some of the presented experimental data were obtained from the previous papers [9, 17] (color online).

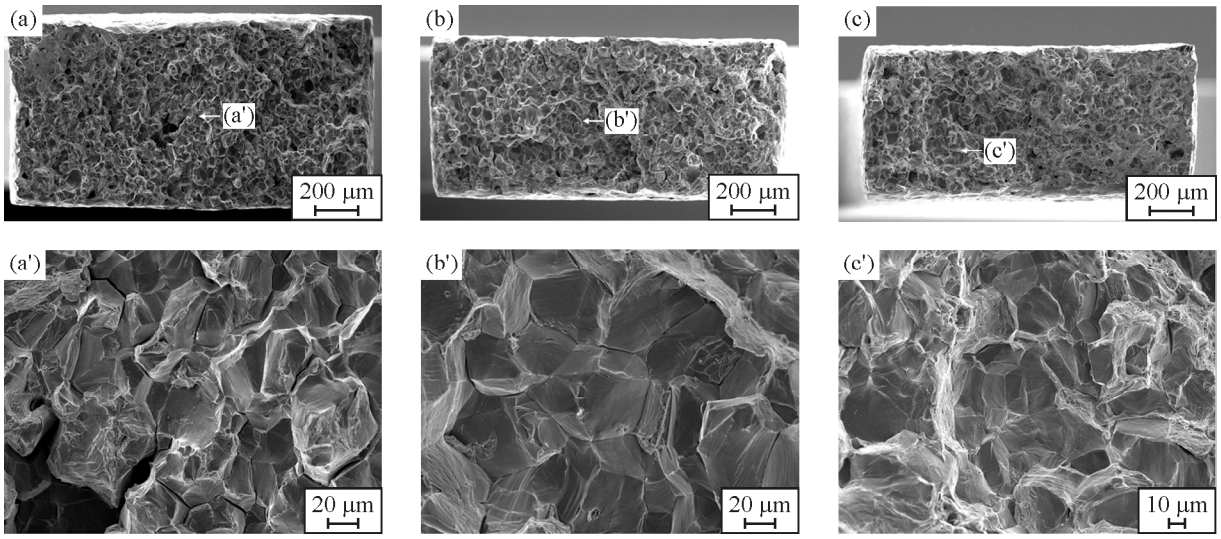

Fig. 2. Overviews (a–c) and magnifications (a′–c′) of the fracture surfaces of hydrogen-charged S-HEA after the tensile tests in Fig. 1: 10^{-4} (a, a′), 10^{-3} (b, b′), and 10^{-2} s^{-1} (c, c′).

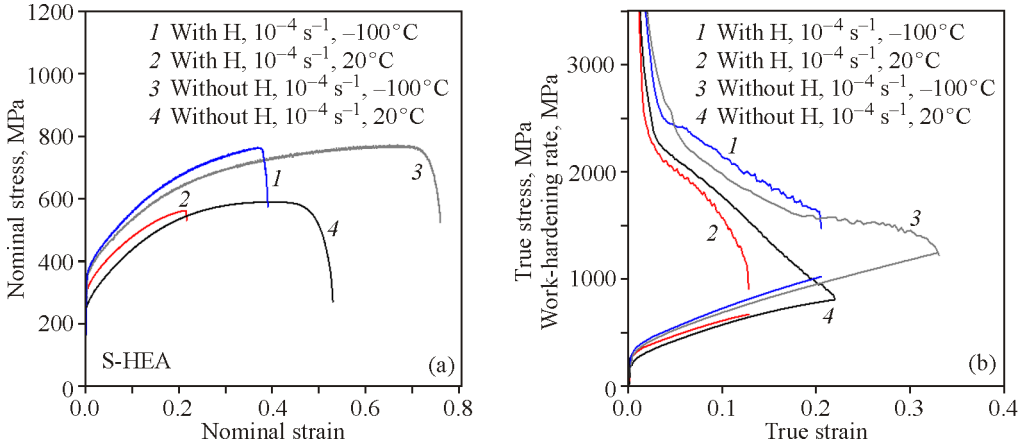

Fig. 3. Low-temperature deformation behavior of S-HEA: nominal stress–strain (a) and work-hardening rate curves (b) (color online).

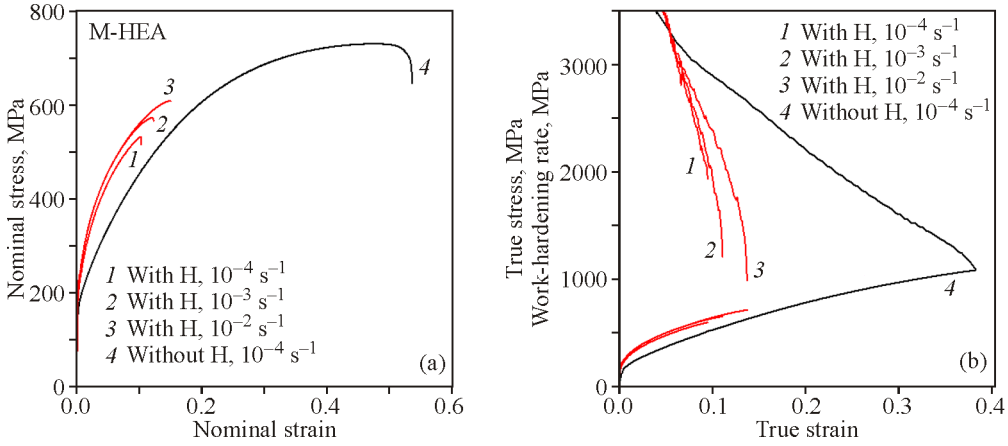

Fig. 4. Nominal stress–strain (a) and work-hardening rate curves (b) at 20°C with and without hydrogen charging in M-HEA. Figure (a) was reproduced from [17] (color online).

unlike the case at 20°C. Fracture at –100°C occurred before the fulfillment of the necking condition. Notably, the elongation of the hydrogen-charged specimen tested at –100°C was larger than that at 20°C.

3.2. Metastable HEA

Figure 4 shows nominal stress–strain curves of M-HEA without and with hydrogen charging. Similar to the behavior of S-HEA, hydrogen charging deteriorated elongation and increased the yield strength. The work hardening rate of hydrogen-charged specimens decreased with decreasing strain rate. Fracture occurred after the fulfillment of the necking condition in the absence of hydrogen, but hydrogen charging caused premature fracture, irrespective of the strain rate. A characteristic feature of hydrogen-charged M-HEA was the insignificant change in the yield strength with increasing strain rate.

As shown in Fig. 5, regardless of the strain rate, hydrogen-charged M-HEA exhibited a quasi-cleavage fracture, although the uncharged specimen exhibited a fully ductile fracture surface [9]. Quasi-cleavage fracture is the typical fracture mode in FCC alloys, in which the FCC–HCP martensitic transformation occurred [19, 20]. Only a minor portion of the fracture surfaces exhibited an intergranular fracture pattern. Consequently, hydrogen charging and decreased strain rate accelerated the occurrence of qua-

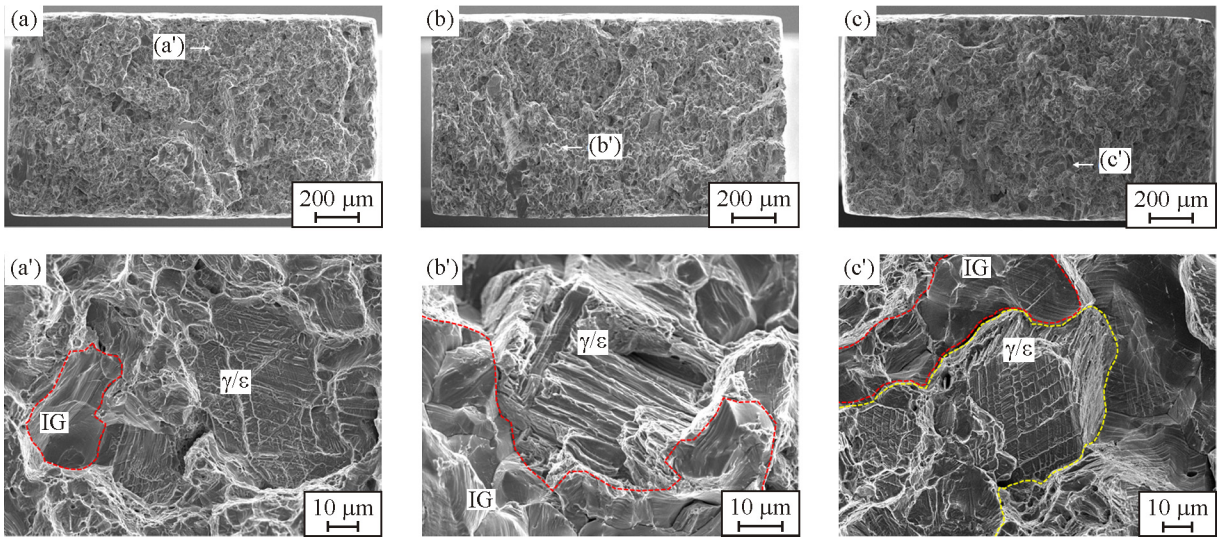

Fig. 5. Overviews (a–c) and magnifications (a′–c′) of the fracture surfaces of hydrogen-charged M-HEA after the tensile tests at 20°C in Fig. 4: 10^{-4} (a, a′), 10^{-3} (b, b′), and 10^{-2} s^{-1} (c, c′). IG—intergranular fracture, γ/ε—interface fracture (color online).

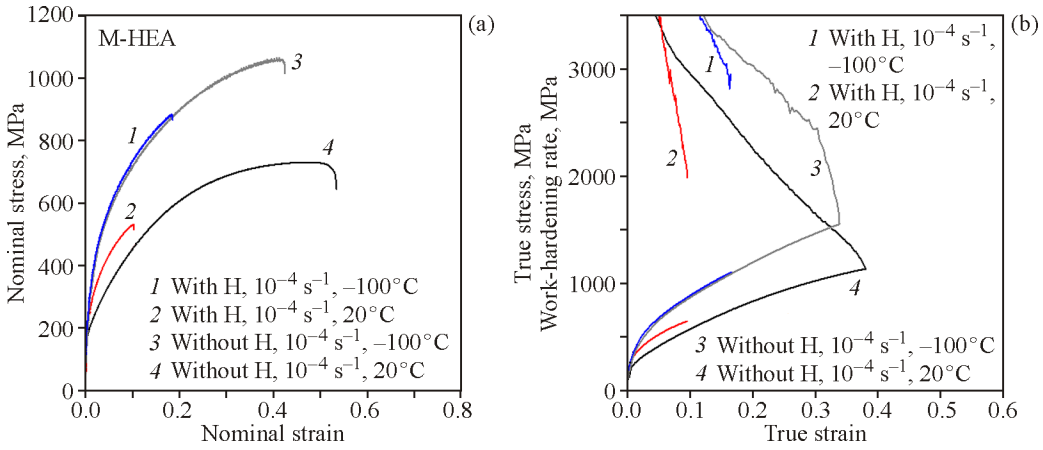

Fig. 6. Low-temperature deformation behavior of M-HEA: nominal stress–strain (a) and work-hardening rate curves (b) (color online).

si-cleavage cracking associated with FCC–HCP martensite. Specifically, step-like ridges on the quasi-cleavage facet of M-HEA indicate the microdamage formation and its growth along the FCC/HCP interfaces [19, 20].

Similar to S-HEA, the elongation of hydrogen-charged M-HEA tested at –100°C was larger than that at 20°C (Fig. 6a). In addition, hydrogen changed insignificantly the stress–strain response until the nominal strain 0.1. Then, the work-hardening rate of hydrogen-charged M-HEA suddenly dropped immediately before fracture (Fig. 6b). When the deformation temperature was decreased to –100°C in M-HEA, quasi-cleavage fracture occurred even when hydrogen was not introduced (Fig. 7a). Furthermore, the topography of step-like ridges became shallow compared to that at 20°C in the hydrogen-charged specimen and at –100°C in the hydrogen-uncharged specimen. Notably, in the hydrogen-charged specimen tested at –100°C, there was a significant fraction of the intergranular fracture surface near the corner of the specimen (Figs. 7b and 7b′), which would be the crack initiation region.

4. DISCUSSION

First, we summarize the results for S-HEA.

Hydrogen charging resulted in an increase in the yield strength at 20°C. The yield strength of hydrogen-charged specimens increased with the strain rate from 10^{-4} to 10^{-2} s^{-1} at 20°C (Fig. 1a). The strain rate effect on the yield strength with hydrogen decreased with decreasing deformation temperature from 20 to –100°C (Fig. 3a).

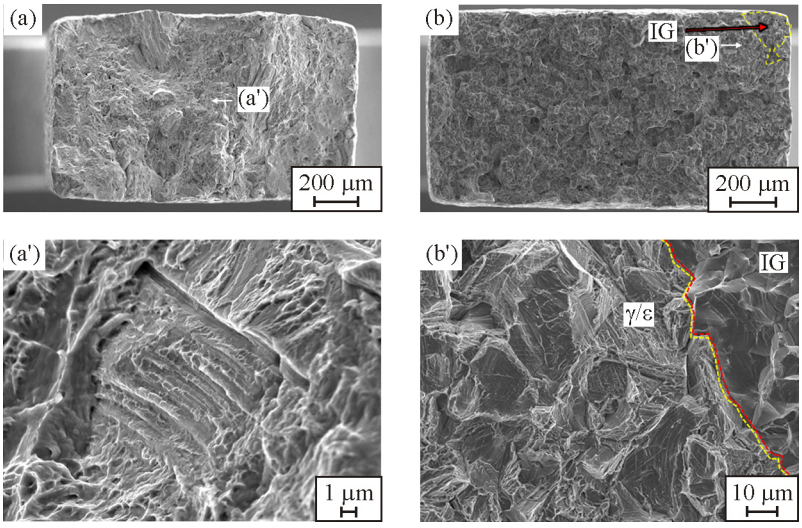

Fig. 7. Overviews (a, b) and magnifications (a′, b′) of the fracture surfaces of hydrogen-uncharged (a, a′) and hydrogen-charged M-HEA (b, b′) after the tensile tests at –100°C in Fig. 6; 10^{-4} s^{-1} (color online).

Intergranular fracture occurred only when plastic strain and hydrogen were provided (Figs. 1a and 2). The stress and strain at which hydrogen-induced intergranular fracture occurred decreased with decreasing strain rate at 20°C (Figs. 1a) and increased with decreasing deformation temperature from 20 to –100°C (Fig. 3a).

Elongation of hydrogen-charged S-HEA at 20°C increased with the strain rate (Fig. 1a), and fracture at 10^{-2} s^{-1} occurred after the fulfillment of the necking condition (Fig. 1b).

The work-hardening rate was decreased by hydrogen charging, particularly at the late stage of plastic deformation at 20°C, and the work-hardening rate changed insignificantly with the variation in the strain rate (Fig. 1b). A decrease in the work-hardening rate by hydrogen was not observed at –100°C (Fig. 3b).

The strain rate effect shown in Fig. 1a indicates that hydrogen atoms preexisting at and around mobile dislocations act as short-range obstacles against dislocation motion, which can be passed through the thermal activation process. For example, lattice distortion and dislocation pinning by solute hydrogen, both of which are dominated by the thermal activation process at room temperature, prevent dislocation motion. However, the temperature effect that reduced the strain rate sensitivity in the hydrogen-charged specimen (Fig. 3a) is unclear, which needs further investigations.

The increase in tensile strength and total elongation with growing strain rate and decreasing temperature in hydrogen-charged specimens, shown in Figs. 1a and 3a, indicates that hydrogen-induced intergranular fracture, observed in Fig. 2, is related to the hydrogen-decorated dislocation motion to grain boundaries. The efficiency of hydrogen delivery by dislocation motion monotonically increases with decreasing strain rate and increasing temperature because of the decrease in dislocation velocity and increase in hydrogen diffusivity. The hydrogen localization at grain boundaries assists the occurrence of intergranular fracture.

The occurrence of intergranular fracture is not a direct factor determining elongation at 10^{-2} s^{-1} and 20°C because fracture occurred after the fulfillment of the necking condition, as shown in Fig. 1b. More specifically, an increase in flow stress and a decrease in work-hardening rate by hydrogen, were direct causes of the hydrogen-induced degradation of elongation at 10^{-2} s^{-1} and 20°C. A reduction in work hardening can be explained by gradual crack/void nucleation during plastic deformation [21]. A gradual increase in the number density and size of cracks/voids decreases macroscopic work hardening rates due to a reduction in the real cross-sectional area of a specimen. The crack/void formation behavior during deformation before fracture should be investigated in the future.

Second, we summarize the results for M-HEA.

Hydrogen charging increased the yield strength of M-HEA, but its degree did not exhibit a significant dependence on the strain rate (Fig. 4a).

Quasi-cleavage fracture occurred as the predominant fracture mode at 20°C in hydrogen-charged M-HEA (Fig. 5). The stress and strain at which hydrogen-induced quasi-cleavage fracture occurred decreased with decreasing strain rate at 20°C (Fig. 4a).

Quasi-cleavage fracture occurred at –100°C even without hydrogen charging (Fig. 7a). Note that quasi-cleavage fracture at –100°C in hydrogen-charged M-HEA occurred at higher stress and strain than that at 20°C (Fig. 6a).

Step-like ridges on the quasi-cleavage facet became shallow when the deformation temperature was decreased from 20 to –100°C in hydrogen-charged M-HEA (Fig. 7b). In addition, an intergranular fracture area was observed in the corner of the specimen.

The yield strength of M-HEA was dominated by the onset of the deformation-induced FCC–HCP martensitic transformation, because the starting temperature for the thermally induced martensitic transformation is 55°C [22]. The critical stress for the deformation-induced FCC–HCP martensitic transformation increases by hydrogen-assisted solution hardening [23], which is consistent with the fact that the yield strength of M-HEA was increased by hydrogen (Fig. 4a). Because the growth of the FCC–HCP martensite resulted from a group motion of dislocations, its growth tip has a larger stress than the stress around a single dislocation. Large stress at the growth tip of the HCP martensite may have decreased the activation volume for dislocation motion in the hydrogen atmosphere, which resulted in the insensitivity of the yield strength to the strain rate in hydrogen-charged M-HEA.

The quasi-cleavage fracture shown in Figs. 5 and 7 is associated with cracking along HCP martensite plates [19, 20]. According to the previous studies, as the flow stress and the amount of the deformation-induced FCC → HCP martensite increase with decreasing temperature, the quasi-cleavage feature becomes distinct at cryogenic temperatures when hydrogen is not considered [24, 25]. However, the de-

crease in temperature in hydrogen-charged specimens increased the critical stress and strain of quasi-cleavage fracture, as shown in Fig. 6. Considering that the strain rate increase also increased the critical stress and strain of quasi-cleavage fracture, the plasticity-related hydrogen transport to the FCC/HCP interface and the interior of the HCP martensite assisted the hydrogen-induced quasi-cleavage fracture at 20°C. Specifically, motions of perfect dislocation and extended dislocation, which act as predominant plasticity mechanisms for the late deformation stage, are considered to transport hydrogen. It is also noteworthy that the temperature decrease in hydrogen-charged specimens increased the ductility (Fig. 6a), but the fracture surface pattern became brittle (elongation became large, but step-like ridges appeared to be shallow) (Fig. 7b). Step-like ridges are formed by the initiation of multiple small cracks/voids and subsequent coalescence along HCP martensite plates [19, 20]. Thus, the position of ridges corresponds to sites of multiple small crack/void initiation, which indicates that shallow step-like ridges in the hydrogen-charged specimen fractured at the low temperature resulted from the crack/void coalescence before the significant opening/growth of cracks/voids. In other words, the plasticity-related hydrogen transport to HCP martensite, which was active at 20°C, contributed to the multiple void/crack initiation, which deteriorated the ductility associated with quasi-cleavage fracture. When the temperature was decreased, the associated increase in flow stress accelerated the coalescence of multiple cracks/voids or grain boundary cracking, which however did not critically deteriorate the ductility at –100°C, because the multiple crack/void initiation originating from the hydrogen transport was suppressed. More specifically, the hydrogen accumulation at the intersections of hydrogen-decorated dislocation motion paths and HCP martensite plates accelerated the crack/void initiation, particularly at 20°C. Considering the variation trend of the mechanical properties by hydrogen charging and at different deformation temperature, the ease of multiple crack/void initiation acted as a detrimental factor causing the failure of hydrogen-charged M-HEA.

5. CONCLUSIONS

As mesoscopic characteristics of hydrogen embrittlement of S-HEA and M-HEA, stress–strain responses and fracture surfaces at different strain rates and temperatures were analyzed. The effects of hydrogen on the mechanical behavior of HEAs can be summarized as follows.

Hydrogen charging of S-HEA increased the yield strength, and the degree increased with increasing strain rate, which indicated that the strengthening mechanism was related to the thermal activation process. The strain rate sensitivity of the yield strength in hydrogen-charged specimens was suppressed when the FCC → HCP martensitic transformation dominated the onset of plasticity (for M-HEA).

At –100°C, the hydrogen effect on the yield strength was observed neither in S-HEA nor in M-HEA. However, further investigation is required to obtain comprehensive understanding.

The combined effects of hydrogen, which increased the flow stress and decreased the work-hardening rate at the late deformation stage in S-HEA, accelerated the occurrence of the specimen necking, particularly at high strain rates, e.g. 10^{-2} s^{-1} at 20°C.

The hydrogen transport to boundaries/interfaces by dislocation motion at the late deformation stages assisted both modes of cracking: along grain boundaries and along HCP martensite plates. The plasticity-related hydrogen transport in M-HEA mainly assisted the crack/void initiation along HCP martensite plates.

FUNDING

This research was funded by JSPS KAKENHI (JP20H02457, JP21K04702) and the Elements Strategy Initiative for Structural Materials (ESISM) of the Ministry of Education, Culture, Sports, Science, and Technology (MEXT) of Japan (JPMXP0112101 000).

REFERENCES

1. Zhang, L., Wen, M., Imade, M., Fukuyama, S., and Yokogawa, K., Effect of Nickel Equivalent on Hydrogen Gas Embrittlement of Austenitic Stainless Steels Based on Type 316 at Low Temperatures, *Acta Mater.*, 2008, vol. 56, pp. 3414–3421. https://doi.org/10.1016/j.actamat.2008.03.022
2. Koyama, M., Twinning-Induced Plasticity (TWIP) Steel, *Encyclopedia of Materials: Metals and Alloys*, 2022, vol. 2, pp. 95–105. https://doi.org/10.1016/b978-0-12-819726-4.00067-3
3. Cantor, B., Multicomponent High-Entropy Cantor Alloys, *Progr. Mater. Sci.*, 2021, vol. 120, p. 100754. https://doi.org/10.1016/j.pmatsci.2020.100754
4. Gludovatz, B., Hohenwarter, A., Catoor, D., Chang, E.H., George, E.P., and Ritchie, R.O., A Fracture-Resistant High-Entropy Alloy for Cryogenic Ap-

plications, *Science*, 2014, vol. 345, pp. 1153–1158. https://doi.org/10.1126/science.1254581
5. Zhao, Y., Lee, D.H., Seok, M.Y., Lee, J.A., Phaniraj, M.P., Suh, J.Y., Ha, H.Y., Kim, J.Y., Ramamurty, U., and Jang, J.I., Resistance of CoCrFeMnNi High-Entropy Alloy to Gaseous Hydrogen Embrittlement, *Scripta Mater*., 2017, vol. 135, pp. 54–58. https://doi.org/10.1016/j.scriptamat.2017.03.029
6. Luo, H., Li, Z., and Raabe, D., Hydrogen Enhances Strength and Ductility of an Equiatomic High-Entropy Alloy, *Sci. Rep*., 2017, vol. 7. https://doi.org/10.1038/s41598-017-10774-4
7. Pu, Z., Chen, Y., and Dai, L. H., Strong Resistance to Hydrogen Embrittlement of High-Entropy Alloy, *Mater. Sci. Eng. A*, 2018, vol. 736, pp. 156–166. https://doi.org/10.1016/j.msea.2018.08.101
8. Nygren, K.E., Bertsch, K.M., Wang, S., Bei, H., Nagao, A., and Robertson, I.M., Hydrogen Embrittlement in Compositionally Complex FeNiCoCrMn FCC Solid Solution Alloy, *Current Opinion Solid State Mater. Sci*., 2018, vol. 22, pp. 1–7. https://doi.org/10.1016/j.cossms.2017.11.002
9. Ichii, K., Koyama, M., Tasan, C.C., and Tsuzaki, K., Comparative Study of Hydrogen Embrittlement in Stable and Metastable High-Entropy Alloys, *Scripta Mater*., 2018, vol. 150, pp. 74–77. https://doi.org/10.1016/j.scriptamat.2018.03.003
10. Wang, H.Y., Koyama, M., Hojo, T., and Akiyama, E., Hydrogen Embrittlement and Associated Surface Crack Growth in Fine-Grained Equiatomic CoCrFeMnNi High-Entropy Alloys with Different Annealing Temperatures Evaluated by Tensile Testing under In Situ Hydrogen Charging, *Int. J. Hydrogen Energy*, 2021, vol. 46, pp. 33028–33038. https://doi.org/10.1016/j.ijhydene.2021.07.136
11. Nygren, K.E., Wang, S., Bertsch, K.M., Bei, H.B., Nagao, A., and Robertson, I.M., Hydrogen Embrittlement of the Equi-Molar FeNiCoCr Alloy, *Acta Mater*., 2018, vol. 157, pp. 218–227. https://doi.org/10.1016/j.actamat.2018.07.032
12. Koyama, M., Wang, H.Y., Verma, V.K., Tsuzaki, K., and Akiyama, E., Effects of Mn Content and Grain Size on Hydrogen Embrittlement Susceptibility of Face-Centered Cubic High-Entropy Alloys, *Metall. Mater. Trans. A*, 2020, vol. 51, pp. 5612–5616. https://doi.org/10.1007/s11661-020-05966-z
13. Koyama, M., Tasan, C.C., and Tsuzaki, K., Overview of Metastability and Compositional Complexity Effects for Hydrogen-Resistant Iron Alloys: Inverse Austenite Stability Effects, *Eng. Fract. Mech.*, 2019, vol. 214, pp. 123–133. https://doi.org/10.1016/j.engfracmech.2019.03.049
14. Hirata, K., Iikubo, S., Koyama, M., Tsuzaki, K., and Ohtani, H., First-Principles Study on Hydrogen Diffusivity in BCC, FCC, and HCP Iron, *Metall. Mater. Trans. A*, 2018, vol. 49, pp. 5015–5022. https://doi.org/10.1007/s11661-018-4815-9
15. Li, Z., Pradeep, K.G., Deng, Y., Raabe, D., and Tasan, C.C., Metastable High-Entropy Dual-Phase Alloys Overcome the Strength–Ductility Trade-Off, *Nature*, 2016, vol. 534, pp. 227–230. https://doi.org/10.1038/nature17981
16. Li, Z.M., Tasan, C.C., Pradeep, K.G., and Raabe, D., A TRIP-Assisted Dual-Phase High-Entropy Alloy: Grain Size and Phase Fraction Effects on Deformation Behavior, *Acta Mater.*, 2017, vol. 131, pp. 323–335. https://doi.org/10.1016/j.actamat.2017.03.069
17. Ichii, K., Koyama, M., Tasan, C.C., and Tsuzaki, K., Localized Plasticity and Associated Cracking in Stable and Metastable High-Entropy Alloys Pre-Charged with Hydrogen, *Proc. Struct. Integr.*, 2018, vol. 13, pp. 716–721. https://doi.org/10.1016/j.prostr.2018.12.119
18. George, E.P., Curtin, W.A., and Tasan, C.C., High Entropy Alloys: A Focused Review of Mechanical Properties and Deformation Mechanisms, *Acta Mater.*, 2020, vol. 188, pp. 435–474. https://doi.org/10.1016/j.actamat.2019.12.015
19. Takaki, S., Furuya, T., and Tokunaga, Y., Effect of Si and Al Additions on the Low Temperature Toughness and Fracture Mode of Fe-27Mn Alloys, *ISIJ Int.*, 1990, vol. 30, pp. 632–638. https://doi.org/10.2355/isijinternational.30.632
20. Hao, C., Koyama, M., and Akiyama, E., Quantitative Evaluation of Hydrogen Effects on Evolutions of Deformation-Induced ε-Martensite and Damage in a High-Mn Steel, *Metall. Mater. Trans. A*, 2020, vol. 51, pp. 6184–6194. https://doi.org/10.1007/s11661-020-06021-7
21. Yang, C.L., Zhang, Z.J., Zhang, P., and Zhang, Z.F., The Premature Necking of Twinning-Induced Plasticity Steels, *Acta Mater.*, 2017, vol. 136, pp. 1–10. https://doi.org/10.1016/j.actamat.2017.06.042
22. Koyama, M., Gondo, T., and Tsuzaki, K., Microstructure Refinement by Low-Temperature Ausforming in a Fe-Based Metastable High-Entropy Alloy, *Metals*, 2021, vol. 11, p. 742. https://doi.org/10.3390/met11050742
23. Koyama, M., Terao, N., and Tsuzaki, K., Revisiting the Effects of Hydrogen on Deformation-Induced γ-ε Martensitic Transformation, *Mater. Lett.*, 2019, vol. 249, pp. 197–200. https://doi.org/10.1016/j.matlet.2019.04.093
24. Sipos, K., Remy, L., and Pineau, A., Influence of Austenite Predeformation on Mechanical Properties and Strain-Induced Martensitic Transformations of a High Manganese Steel, *Metall. Trans. A*, 1976, vol. 7, pp. 857–864. https://doi.org/10.1007/Bf02644083
25. Koyama, M., Kaneko, T., Sawaguchi, T., and Tsuzaki, K., Microstructural Damage Evolution and Arrest in Binary Fe–High-Mn Alloys with Different Deformation Temperatures, *Int. J. Fracture*, 2018, vol. 213, pp. 193–206. https://doi.org/10.1007/s10704-018-0307-6